GEOPHYSICS, VOL. 85, NO. 6 (NOVEMBER-DECEMBER 2020); P. D233–D243, 5 FIGS.
10.1190/GEO2020-0163.1

Check for updates

Downloaded 11/15/20 to 177.65.175.205. Redistribution subject to SEG license or copyright; see Terms of Use at https://library.seg.org/page/policies/terms
DOI:10.1190/geo2020-0163.1

A new look at the causes of "polarization" horns in electromagnetic well logging

Cícero Régis[1], Paulo Roberto de Carvalho[2], and Valdelírio da Silva e Silva[3]

ABSTRACT

So-called polarization horns appear in electromagnetic well logs when the sondes move through the interface between formations of different conductivities. Since the early 1990s, peaks in the logs have been attributed to the influence of surface charges due to the presence of electric field components perpendicular to the interfaces. A new analysis finds that surface charges should not be pinpointed as the immediate cause for the appearance of interface peaks in electromagnetic logs from any tool operating in any frequency range. This is accomplished by calculating the derivatives of the magnetic field components with respect to the sonde's vertical position as it crosses the interface between two homogeneous isotropic media. The mathematical expressions reveal the components with smooth transitions and the ones with discontinuities in their rates of change across the interface. The analysis is applied to the four components needed to simulate the responses of coaxial and coplanar coil configurations in dipping logs. The results show that only the horizontal field from a horizontal dipole source suffers an influence from the current density field perpendicular to the interface between the two media, which gives rise to surface charges, but even for this component, the nonsmooth transitions are not associated with the perpendicular current. An anisotropic example gives further support to the conclusion that the *polarization* horns are associated with the discontinuous current density field parallel to the interface rather than with the continuous current across the interface.

INTRODUCTION

Electromagnetic well logging was originally performed exclusively in vertical wells using the coaxial source-receiver configuration. The calculation of apparent resistivities and the modeling of the data were performed only with the vertical magnetic component generated by a vertical magnetic dipole (VMD). Later, when coaxial tools started to be used in inclined wells, and later still, in the 1990s, when the first experiments were carried out with the coplanar configuration to resolve anisotropy in thinly laminated formations, the horizontal magnetic dipole (HMD) source started to be used in the calculations and in the sondes.

In dipping wells profiled with any configuration and in vertical wells profiled with coplanar configurations, the logs started to show strong spikes as the sondes crossed the interfaces between formations with different conductivities. At first, these "horns" were considered an inconvenience; they were even called "undesirable artifacts" (Moran and Gianzero, 1979) because boundary effects were known to induce apparent resistivity responses not corresponding to any resistivity in a heterogeneous medium. According to Kriegshäuser et al. (2000), "the induction response of the new coplanar coils is complex and sometimes not intuitive. Borehole and eccentricity effects can distort the new coplanar responses more than conventional coaxial induction coil responses."

Anderson et al. (1992) show a classic North Sea field log example that illustrates how an unexpected horn on 2 MHz logging while drilling (LWD) logs turned out to be a useful indicator of bed boundary crossings in highly deviated wells. In this case, the computed log was modeled first, before the well was drilled, so it could be used to confirm that it was possible to identify the position where the tool crossed the interface between a 1.0 ohm-m shale and an 1000 ohm-m gas sand in a 72° deviated well. The subsequent field

Manuscript received by the Editor 15 March 2020; revised manuscript received 20 July 2020; published ahead of production 2 October 2020; published online 10 November 2020.
[1]Federal University of Pará, Graduate Program in Geophysics, R. Augusto Correa, 01, Belém 66075-110, Brazil and National Institute of Science and Technology of Petroleum Geophysics, Salvador 40170-115, Brazil. E-mail: cicero@ufpa.br (corresponding author).
[2]Federal Rural University of the Amazon, Cyberspace Institute, Av. Perimetral, 2501, Belém 66095-780, Brazil. E-mail: prdcarvalhoufra@gmail.com.
[3]Federal University of Pará, Faculty of Mathematics, Av. dos Universitários, Castanhal 68746-360, Brazil. E-mail: valdel@ufpa.br.
© 2020 Society of Exploration Geophysicists. All rights reserved.

Downloaded 11/15/20 to 177.65.175.205. Redistribution subject to SEG license or copyright; see Terms of Use at https://library.seg.org/page/policies/terms
DOI:10.1190/geo2020-0163.1

log is in good agreement with the modeled results, showing a horn associated with the boundary as a real feature and not an isolated tool artifact or computer modeling effect (Anderson, 2019).

With time, as dipping wells became common and as the use of coaxial and coplanar configurations became important in the application to anisotropic formations, the spikes started to be taken as an unavoidable part of the logs, and they were even interpreted as useful boundary markers. Currently, the horns in LWD logs are an important guide to correct the drilling in real-time geosteering and keep the well horizontal within the target layer (Pitcher et al., 2011). They are now recognized as a general feature of induction logs, not restricted to any particular tool configuration.

In the interpretation of the physical causes of the horns, a critical observation was that the spikes in the resistivity logs appeared only in situations in which electric field lines crossed the interfaces, which did not happen in coaxial logs in vertical wells. Based on this behavior, Howard and Chew (1989, 1992) present the first interpretation of the horns as a consequence of the bed boundary charge buildup, or polarization, associated with the electric field component perpendicular to the interfaces between formations. They describe the surface charges due to the dipole sources and assumed that the nonsmooth behavior of the logs was exclusively due to these surface charges. Since then, these spikes in the logs have been known as *polarization horns*, and it has been universally accepted that their causes are the surface charges.

Here, we present an analysis that demonstrates that spikes in the plots of the magnetic field components of magnetic dipole sources may appear in situations in which there are no electric field lines crossing any interface, therefore no surface charges. It is also shown that, even in cases in which there are surface charges involved, the horns may not be attributed to them.

An analysis of the physics of the flow of currents that generate the observed magnetic fields allows the conclusion that the nonsmooth behavior of the magnetic components is due to the discontinuities in the current density vector field parallel to the interfaces, which imply continuous electric field components parallel to the same boundary, rather than those in the electric field perpendicular to the interface, which are associated with continuous current density across the same boundary and which give rise to surface charges.

MODEL CASE

The simplest situation to be studied is that of two homogeneous isotropic half-spaces separated by a horizontal plane interface, without the presence of the borehole and invasion zones, to simulate deviated logs with respect to a horizontal bed boundary. According to Anderson et al. (1992), the horn spikes appear sharper in this situation than in the real logs. This 1D simple model provides basic insight for understanding tool responses in more complex scenarios.

The building blocks for the modern multicomponent induction tools are the basic coaxial and coplanar two-coil arrays, to which is added a third so-called bucking coil to cancel the direct linkage, or mutual coupling (Kaufman and Ytskovich, 2017). The dipole source in each case points in a direction that depends on the dip angle: The dipole moment vector of the source in a coaxial array points in the direction of the profile, whereas the source in a coplanar array has a dipole moment perpendicular to the profile line. However, to simulate a measurement of any induction logging tool, operating in any frequency range, it is enough to calculate the responses of HMD and VMD sources and combine the horizontal and vertical magnetic components generated by both sources in the point receiver position, taking into account the deviation angle of the well. Therefore, the analysis presented here focuses on four configurations: vertical and horizontal magnetic components generated by VMD and HMD.

As a further reduction in the problem, the following calculations assume, without loss of generality for the horizontally layered 1D case, that the log profile is on the (x, z)-plane at $y = 0$. The tilt angle θ of the profile is measured in relation to the vertical z-axis. A magnetic component at the receiver position is represented by H_{ij}, with i indicating the direction (x or z) of the source dipole and j indicating the direction of the field component.

The observed fields for the coaxial (CX) and coplanar (CP) coil configurations, with source dipole moments m, are the combination of four signals, originating from two unit dipoles:

$$H_{\mathrm{CX}} = m(H_{xx}\sin^2\theta + H_{xz}\sin\theta\cos\theta + H_{zx}\sin\theta\cos\theta + H_{zz}\cos^2\theta), \quad (1)$$

$$H_{\mathrm{CP}} = m(H_{xx}\cos^2\theta - H_{xz}\sin\theta\cos\theta - H_{zx}\sin\theta\cos\theta + H_{zz}\sin^2\theta). \quad (2)$$

The next sections will study these four signals separately to determine each contribution to the behavior of the total fields. The analysis determines the behavior of the magnetic field in two situations, during the transitions of the transmitter and the receiver through the interface between the two half-spaces. To facilitate the interpretation of the logs of the illustration example, all points in the curves are plotted at the position of the receiver. This is contrary to the usual practice of plotting the measurements at the midpoint between the transmitter and the receiver, but the resulting plots have the advantage of exactly locating the discontinuities in the rate of change of the fields as the tool moves across the interface.

To illustrate the behavior of all components involved in a wireline induction log example, the following curves were generated for a two half-space model with top and bottom conductivities of $\sigma_1 = 0.01$ S/m and $\sigma_2 = 1.0$ S/m, respectively, and the same relative electric permittivity or dielectric constant $\varepsilon_r = 1$. The profile runs at a dip angle $\theta = 60°$ with the vertical direction and with a source dipole moment of $1.0\,\mathrm{Am}^2$ at 20 kHz. The separation between the source and receiver is $L = 1.0$ m. Figure 1 shows the coaxial and coplanar profiles for this model.

Nonsmooth transitions are observed in all four curves, meaning that there are discontinuities in the rates of change of the magnetic field components in the tool positions where the receiver crosses the interface as well as where the transmitter crosses the interface. Of particular interest are the curves of the imaginary component because they are the ones used to calculate the raw apparent conductivities.

Although this model is used to illustrate the behavior of the fields in an ordinary environment, the conclusions will not be drawn from the study of this or any particular case, but rather from the analysis of the general expressions for the rate of change of the fields at the interface, which are valid for any range of frequency as long as the continuity of the current density field normal to the interface is valid.

Downloaded 11/15/20 to 177.65.175.205. Redistribution subject to SEG license or copyright; see Terms of Use at https://library.seg.org/page/policies/terms
DOI:10.1190/geo2020-0163.1

CALCULATIONS

In an electromagnetic problem, the magnetic field is created by the flow of current in the medium in two forms: conduction and displacement currents, of which the density vector fields are jointly expressed in the frequency domain as $\mathcal{J} = (\sigma + i\omega\varepsilon_0\varepsilon_r)\mathbf{E}$. This linear constitutive relation between the electric and the current density fields holds for all of the field intensities and in the media involved in any electromagnetic logging tool. The term

$$\eta_j = \sigma_j + i\omega\varepsilon_0\varepsilon_{r(j)} \tag{3}$$

is called the admittivity of medium j (Harrington, 2001, p. 19). Notice that the following calculation remains unchanged even in dispersive cases in which the conductivity and the permittivity may be complex functions of the frequency.

In many applications that work in the quasistatic regime, the admittivity is approximated by the conductivity because the $i\omega\varepsilon_0\varepsilon_r$ term is very small. In the applications of electromagnetic well logging, however, the frequency may reach the MHz range, as in the case of LWD, and the sondes may encounter formations with high relative electric permittivity ε_r. Therefore, the formulation in this theoretical study must use the complete expression for the admittivity, so that it may be applied to any range of frequency used in the actual tools.

A central point in this analysis is that, at any point of the interface between the two media ($z = 0$), the component of the total current density field perpendicular to the interface is continuous (Ward and Hohmann, 1987; for a more detailed discussion, see Kaufman and Ytskovich, 2017):

$$\mathcal{J}_z = \eta_1 E_{z(1)} = \eta_2 E_{z(2)} \quad (z = 0). \tag{4}$$

Therefore, the normal electric field is discontinuous, such that the ratio of the field immediately above and immediately below the interface is

$$\left.\frac{E_{z(1)}}{E_{z(2)}}\right|_{z=0} = \frac{\eta_2}{\eta_1}. \tag{5}$$

The current density tangential to the interface ($\mathcal{J}_x$) is discontinuous, such that the ratio of the current immediately above and below the interface is the same as the contrast ratio of the electrical properties (admittivity) of the two media,

$$\left.\frac{\mathcal{J}_{x(1)}}{\mathcal{J}_{x(2)}}\right|_{z=0} = \frac{\eta_1}{\eta_2}, \tag{6}$$

and the tangent electric field is always continuous (Harrington, 2001, p. 34).

In view of these boundary (or interface) conditions, we would expect the nonsmooth characteristics of the logs to be associated with the horizontal rather than with the vertical component of the current in our plane interface model. These considerations lead to a conclusion that is contrary to the view that surface charge buildup determines the nonsmooth behavior of the magnetic field observed in the induction tool responses. To investigate this, we calculate the rate of change of each magnetic component as the tool moves across the interface.

The magnetic field components of both dipole sources are calculated using the mathematical tools described by Ward and Hohmann (1987). The analytical solutions for the three positions shown in Figure 2 are written as integrals of the Hankel transform, which must be evaluated numerically.

The field from the vertical dipole propagates exclusively in the transverse electric mode in relation to the z-axis (TE_z), which means that all electric field lines are parallel to the horizontal interface and no surface charges appear anywhere.

Using Schelkunoff potentials, the field from the HMD can be written as the combination of a TE_z and a transverse magnetic (TM_z) mode propagations. The solutions for the vertical H_{xz} component involve only the TE_z mode, whereas the horizontal H_{xx} component is written as the sum of integrals for the TE_z and the TM_z modes.

The H_{xx} component generated by the HMD_x is the only one of the four considered here that suffers the influence of the vertical components of the electric field and current density. Therefore, this is the only component with which surface charges may be involved.

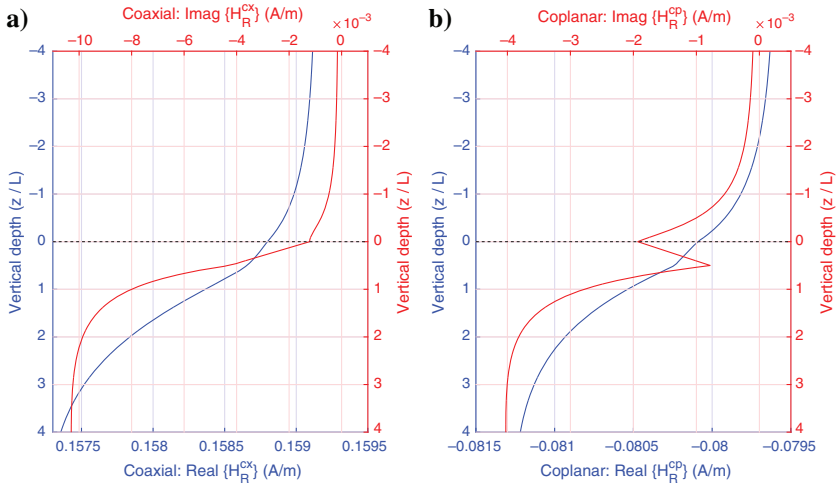

Figure 1. Coaxial and coplanar logs of the magnetic field from unit dipole sources at 20 kHz, source/receiver spacing $L = 1.0$ m, dip angle of 60°, for a two-half-space model with conductivities of $\sigma_{top} = \sigma_1 = 0.01$ S/m and $\sigma_{bottom} = \sigma_2 = 1.0$ S/m.

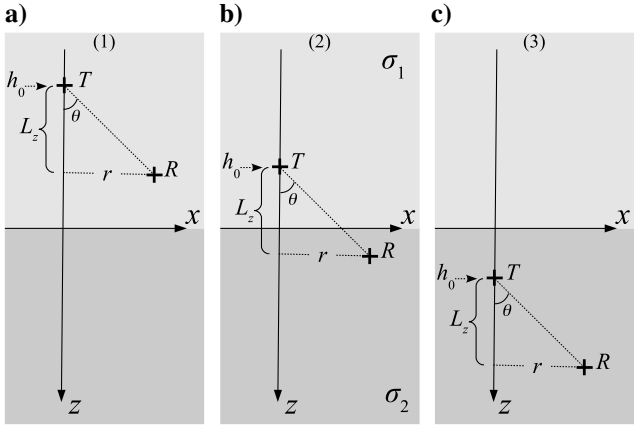

Figure 2. Three positions of the transmitter-receiver pair as the sonde crosses the interface: (a) position 1, (b) position 2, and (c) position 3.

Downloaded 11/15/20 to 177.65.175.205. Redistribution subject to SEG license or copyright; see Terms of Use at https://library.seg.org/page/policies/terms
DOI:10.1190/geo2020-0163.1

The formulation uses the same notation as in Ward and Hohmann (1987), with a time factor $e^{i\omega t}$. Both half-spaces are assumed to have the same vacuum magnetic permeability μ_0. Attributing the same permeability to both media insures that all magnetic components are continuous at the interface. The formulas are expressed in terms of the following parameters:

h_0 is the z-coordinate of the dipole source;
m is the dipole moment of the source;
θ is the dip angle;
$L_z = L\cos\theta$ is the vertical separation between source and receiver;
r is the horizontal separation between source and receiver;
σ_1 and σ_2 are the top and bottom conductivities, respectively;
η_j is the admittivity of medium j: $\eta_j = \sigma_j + i\omega\varepsilon_0\varepsilon_{r(j)}$;
k_j is the wavenumber for medium j: $k_j^2 = -i\omega\mu_0\eta_j$;
λ is the variable of integration of the Hankel transform.
$u_j^2 = \lambda^2 - k_j^2$;
$\mathcal{Y}_j = \frac{u_j}{i\omega\mu_0}$ is the admittance of medium j;
$\mathcal{Z}_j = \frac{u_j}{\eta_j}$ is the impedance of medium j;
$R_{\mathrm{TE}} = \frac{\mathcal{Y}_1 - \mathcal{Y}_2}{\mathcal{Y}_1 + \mathcal{Y}_2} = \frac{u_1 - u_2}{u_1 + u_2}$, for $\mu_1 = \mu_2 = \mu_0$;
$R_{\mathrm{TM}} = \frac{\mathcal{Z}_1 - \mathcal{Z}_2}{\mathcal{Z}_1 + \mathcal{Z}_2}$.

The last two are the reflection coefficients associated with the field propagating from medium 1 to medium 2. The expressions for the contributions of the TE_z mode fields depend only on the admittances of the media, whereas those of the TM_z mode fields depend only on the impedances.

To indicate one of the three positions illustrated in Figure 2, the magnetic component at the receiver position is represented with a superscript $H_{ij}^{(k)}$ ($k = 1, 2$, or 3). In all cases, the arguments of these functions indicate the coordinates (r, z) and the source position (h_0), so the complete representation is $H_{ij}^{(k)}(r, z; h_0)$.

This section presents the analysis of the final expressions for the derivatives of the magnetic components with respect to the source position h_0 at the coordinates of the receiver crossing ($h_0 = -L_z$) and the transmitter crossing ($h_0 = 0$) the interface. The intermediate steps in the derivation are presented in Appendix A.

Fields of the VMD

A VMD transmitter in a horizontally layered medium generates three field components with perfect cylindrical symmetry: the azimuthal electric field, and two (radial and vertical) magnetic components. The electric field lines are horizontal circles concentric with the dipole source. There is no component of the electric field normal to the interface. The fields propagate only in the TE_z mode.

Vertical magnetic component of the VMD

The receiver crosses the interface when the transmitter is at $h_0 = -L_z$ and the transmitter crosses the interface at $h_0 = 0$. In both cases, the rates of change of H_z immediately before and after the interface are the same:

$$\left.\frac{\partial}{\partial h_0}H_{zz}^{(1)}(r,h_0+L_z;h_0)\right|_{h_0=-L_z} = \left.\frac{\partial}{\partial h_0}H_{zz}^{(2)}(r,h_0+L_z;h_0)\right|_{h_0=-L_z}$$
$$= \frac{m}{2\pi}\int_0^\infty R_{\mathrm{TE}}e^{-u_1L_z}\mathrm{J}_0(\lambda r)\lambda^3 d\lambda, \tag{7}$$

$$\left.\frac{\partial}{\partial h_0}H_{zz}^{(2)}(r,h_0+L_z;h_0)\right|_{h_0=0} = \left.\frac{\partial}{\partial h_0}H_{zz}^{(3)}(r,h_0+L_z;h_0)\right|_{h_0=0}$$
$$= \frac{m}{2\pi}\int_0^\infty R_{\mathrm{TE}}e^{-u_2L_z}\mathrm{J}_0(\lambda r)\lambda^3 d\lambda. \tag{8}$$

These equalities indicate that the profile curve for the H_{zz} component of the VMD is always smooth as the sonde crosses the interface, regardless of the dip angle of the well.

Horizontal magnetic component of the VMD

As the receiver crosses the interface ($h_0 = -L_z$), the rate of change of H_{zx} changes discontinuously:

$$\left.\frac{\partial}{\partial h_0}H_{zx}^{(1)}(r,h_0+L_z;h_0)\right|_{h_0=-L_z} = \frac{-m}{2\pi}\int_0^\infty u_1R_{\mathrm{TE}}e^{-u_1L_z}\mathrm{J}_1(\lambda r)\lambda^2 d\lambda, \tag{9}$$

$$\left.\frac{\partial}{\partial h_0}H_{zx}^{(2)}(r,h_0+L_z;h_0)\right|_{h_0=-L_z} = \frac{m}{2\pi}\int_0^\infty u_2R_{\mathrm{TE}}e^{-u_1L_z}\mathrm{J}_1(\lambda r)\lambda^2 d\lambda. \tag{10}$$

The derivatives are different by the factor u_j in the integrands ($-u_1$ above the interface and u_2 below it). Therefore, the expressions for the rates of change of the field (equations 9 and 10) demonstrate that the curve for H_{zx} will not have a smooth transition between the two media. Depending on the resistivities and frequency, the profile curve as the receiver crosses the interface will show either a sharp kink (when the two derivatives have the same sign), or a true spike (a horn shape, when the derivatives have opposite signs), even though in the case of the VMD there is absolutely no surface charge.

The rates of change for cases 1 and 2 (equations A-14 and A-15) can be written as the sum of two signals, one that changes smoothly and one with a discontinuity at the interface. Start by opening up the expression for the reflection coefficient:

$$u_1R_{\mathrm{TE}} = \frac{u_1^2}{u_1+u_2} - \frac{u_1u_2}{u_1+u_2}, \tag{11}$$

$$u_2R_{\mathrm{TE}} = \frac{u_1u_2}{u_1+u_2} - \frac{u_2^2}{u_1+u_2}. \tag{12}$$

Then, use $u_j^2 = \lambda^2 - k_j^2 = \lambda^2 + i\omega\mu_0\eta_j$ and arrive at

$$\frac{\partial}{\partial h_0}H_{zx}^{(1)}(r,h_0+L_z;h_0) = \frac{m}{2\pi}\left[\int_0^\infty \frac{u_1u_2-\lambda^2}{u_1+u_2}e^{u_1(2h_0+L_z)}\mathrm{J}_1(\lambda r)\lambda^2 d\lambda - \eta_1\int_0^\infty \frac{i\omega\mu_0}{u_1+u_2}e^{-u_1L_z}\mathrm{J}_1(\lambda r)\lambda^2 d\lambda\right], \tag{13}$$

Downloaded 11/15/20 to 177.65.175.205. Redistribution subject to SEG license or copyright; see Terms of Use at https://library.seg.org/page/policies/terms
DOI:10.1190/geo2020-0163.1

$$\frac{\partial}{\partial h_0}H_{zx}^{(2)}(r,h_0+L_z;h_0)$$
$$=\frac{m}{2\pi}\left[\int_0^\infty \frac{u_1u_2-\lambda^2}{u_1+u_2}e^{u_1h_0}e^{-u_2(h_0+L_z)}\mathrm{J}_1(\lambda r)\lambda^2 d\lambda\right.$$
$$\left.-\eta_2\int_0^\infty \frac{i\omega\mu_0}{u_1+u_2}e^{-u_1L_z}\mathrm{J}_1(\lambda r)\lambda^2 d\lambda\right]. \quad (14)$$

When the receiver is at the interface ($h_0=-L_z$),

$$\left.\frac{\partial}{\partial h_0}H_{zx}^{(1)}(r,h_0+L_z;h_0)\right|_{h_0=-L_z}$$
$$=\frac{m}{2\pi}\left[\int_0^\infty \frac{u_1u_2-\lambda^2}{u_1+u_2}e^{-u_1L_z}\mathrm{J}_1(\lambda r)\lambda^2 d\lambda\right.$$
$$\left.-\eta_1\int_0^\infty \frac{i\omega\mu_0}{u_1+u_2}e^{-u_1L_z}\mathrm{J}_1(\lambda r)\lambda^2 d\lambda\right], \quad (15)$$

$$\left.\frac{\partial}{\partial h_0}H_{zx}^{(2)}(r,h_0+L_z;h_0)\right|_{h_0=-L_z}$$
$$=\frac{m}{2\pi}\left[\int_0^\infty \frac{u_1u_2-\lambda^2}{u_1+u_2}e^{-u_1L_z}\mathrm{J}_1(\lambda r)\lambda^2 d\lambda\right.$$
$$\left.-\eta_2\int_0^\infty \frac{i\omega\mu_0}{u_1+u_2}e^{-u_1L_z}\mathrm{J}_1(\lambda r)\lambda^2 d\lambda\right]. \quad (16)$$

The second term in these expressions (the one that imposes the discontinuity in the rate of change of the field) differs from case 1 to case 2 only by the η_j factor multiplying the same integral. The ratio of this term in both cases at the interface (η_1/η_2) is the same ratio of the horizontal component of the current density field immediately above and below the interface (equation 6).

As the vertical dipole transmitter crosses the interface ($h_0=0$), the horizontal H_{zx} component presents a smooth transition:

$$\left.\frac{\partial}{\partial h_0}H_{zx}^{(2)}(r,h_0+L_z;h_0)\right|_{h_0=0}=\left.\frac{\partial}{\partial h_0}H_{zx}^{(3)}(r,h_0+L_z;h_0)\right|_{h_0=0}$$
$$=\int_0^\infty u_2R_{\mathrm{TE}}e^{-u_2L_z}\mathrm{J}_1(\lambda r)\lambda^2 d\lambda. \quad (17)$$

To illustrate these behaviors, Figure 3 shows a plot of both magnetic components from a unit VMD, calculated for the two-half-space model (Figure 2) with the same parameters as those used to generate the logs in Figure 1. In this case, the curves for H_{zz} exhibit the expected smooth behavior and those for H_{zx} show the horn shape, even with no surface charges appearing anywhere.

Fields of the HMD$_x$

The transmitter now is an HMD source with a dipole moment oriented along the x-axis. In this case, there are electric field lines crossing the interface, giving rise to surface charges resulting from the necessity for continuity of the normal component of the current density field, which is demanded by the conservation of electric charge.

Vertical magnetic component of the HMD$_x$

Observing the contributions of the two propagation modes, one finds out that the vertical H_{xz} component depends exclusively on the TE$_z$ mode, which means that it is created by the parts of the flow of currents that are always parallel to the interface: again, no surface charges involved.

Now, H_{xz} has a smooth transition as the receiver crosses the interface ($h_0=-L_z$):

$$\left.\frac{\partial}{\partial h_0}H_{xz}^{(1)}(r,h_0+L_z;h_0)\right|_{h_0=-L_z}=\left.\frac{\partial}{\partial h_0}H_{xz}^{(2)}(r,h_0+L_z;h_0)\right|_{h_0=-L_z}$$
$$=\frac{m}{2\pi}\int_0^\infty u_1R_{\mathrm{TE}}e^{-u_1L_z}\mathrm{J}_1(\lambda r)\lambda^2 d\lambda. \quad (18)$$

When the source crosses the interface ($h_0=0$), the derivatives are

$$\left.\frac{\partial}{\partial h_0}H_{xz}^{(2)}(r,h_0+L_z;h_0)\right|_{h_0=0}$$
$$=\frac{m}{2\pi}\int_0^\infty u_1R_{\mathrm{TE}}e^{-u_2L_z}\mathrm{J}_1(\lambda r)\lambda^2 d\lambda, \quad (19)$$

$$\left.\frac{\partial}{\partial h_0}H_{xz}^{(3)}(r,h_0+L_z;h_0)\right|_{h_0=0}$$
$$=\frac{-m}{2\pi}\int_0^\infty u_2R_{\mathrm{TE}}e^{-u_2L_z}\mathrm{J}_1(\lambda r)\lambda^2 d\lambda. \quad (20)$$

Again, we find the same expressions except for the u_1 and $-u_2$ terms in the integrands. So, there is a nonsmooth transition, a discontinuity in the rate of change of the field as the transmitter crosses the interface. This discontinuity will manifest itself either as a sharp bend or a horn shape in the log. Furthermore, repeating the same steps as in the case of the horizontal (H_{zx}) component of the vertical dipole source (equations 11–16), these derivatives can be written as the sum of a smooth signal and a discontinuous one for which the discontinuity ratio is again the same as that of the tangent component of the current density field: η_1/η_2 (equation 6).

The results for the H_{xz} component of the HMD$_x$ could be deduced from symmetry and reciprocity considerations applied to the H_{zx} field from the VMD.

Horizontal magnetic component of the HMD$_x$

The horizontal component (H_{xx}) generated by the HMD$_x$ is written as the sum of the separate contributions of the TE$_z$ and TM$_z$ propagation modes. In the general situations in which $y\neq 0$, the TM$_z$ contribution is written as the sum of two integrals, involving J_0 and J_1, but for $y=0$ only the J_1 integral is present.

Repeating the same procedure as previously, the rates of change of the H_{xx} field with respect to h_0 are as follows:

Downloaded 11/15/20 to 177.65.175.205. Redistribution subject to SEG license or copyright; see Terms of Use at https://library.seg.org/page/policies/terms
DOI:10.1190/geo2020-0163.1

for the receiver crossing the interface ($h_0 = -L_z$),

$$\frac{\partial}{\partial h_0} H_{xx}^{(1)}(r, h_0 + L_z; h_0)\Big|_{h_0=-L_z} = \frac{m}{2\pi r}\left\{\int_0^\infty k_1^2 R_{\mathrm{TM}} e^{-u_1 L_z} \mathrm{J}_1(\lambda r) d\lambda - \int_0^\infty u_1^2 R_{\mathrm{TE}} e^{-u_1 L_z} \mathrm{J}_1(\lambda r) d\lambda + r\int_0^\infty u_1^2 R_{\mathrm{TE}} e^{-u_1 L_z} \mathrm{J}_0(\lambda r)\lambda d\lambda\right\}, \quad (21)$$

$$\frac{\partial}{\partial h_0} H_{xx}^{(2)}(r, h_0 + L_z; h_0)\Big|_{h_0=-L_z} = \frac{m}{2\pi r}\left\{\int_0^\infty \frac{k_1^2(u_1 - u_2)}{\eta_1(\mathcal{Z}_1 + \mathcal{Z}_2)} e^{-u_1 L_z} \mathrm{J}_1(\lambda r) d\lambda + \int_0^\infty u_1 u_2 R_{\mathrm{TE}} e^{-u_1 L_z} \mathrm{J}_1(\lambda r) d\lambda - r\int_0^\infty u_1 u_2 R_{\mathrm{TE}} e^{-u_1 L_z} \mathrm{J}_0(\lambda r)\lambda d\lambda\right\}. \quad (22)$$

The equations show that the TE_z contribution, which does not suffer the influence of surface charges, presents the same characteristics found in the previous components, indicating the nonsmooth transition, or discontinuity in the rate of change of the function: the expressions for the derivatives immediately above and below the interface are the same, except for the different u_j terms in the integrands and the sign reversal. In addition, by performing the same separation of the $u_j R_{\mathrm{TE}}$ term as in the case of the H_{zx} component, the same ratio (η_1/η_2) is found between the discontinuous part of the derivative from the two cases.

For the analysis of the TM contribution, which does suffer the influence of surface charges, the expressions for the two sonde positions (equations 21 and 22) can be written as the sums of two parts by separating the fractions involving $(u_1 - u_2)$ in the two cases:

case 1:

$$\int_0^\infty k_1^2 R_{\mathrm{TM}} e^{-u_1 L_z} \mathrm{J}_1(\lambda r) d\lambda = \int_0^\infty k_1^2 \frac{\mathcal{Z}_1}{(\mathcal{Z}_1 + \mathcal{Z}_2)} e^{-u_1 L_z} \mathrm{J}_1(\lambda r) d\lambda - \frac{1}{\eta_2}\int_0^\infty k_1^2 \frac{u_2}{(\mathcal{Z}_1 + \mathcal{Z}_2)} e^{-u_1 L_z} \mathrm{J}_1(\lambda r) d\lambda; \quad (23)$$

case 2:

$$\int_0^\infty \frac{k_1^2(u_1 - u_2)}{\eta_1(\mathcal{Z}_1 + \mathcal{Z}_2)} e^{-u_1 L_z} \mathrm{J}_1(\lambda r) d\lambda = \int_0^\infty k_1^2 \frac{\mathcal{Z}_1}{(\mathcal{Z}_1 + \mathcal{Z}_2)} e^{-u_1 L_z} \mathrm{J}_1(\lambda r) d\lambda - \frac{1}{\eta_1}\int_0^\infty k_1^2 \frac{u_2}{(\mathcal{Z}_1 + \mathcal{Z}_2)} e^{-u_1 L_z} \mathrm{J}_1(\lambda r) d\lambda. \quad (24)$$

The first part is exactly the same in both sonde positions, whereas in the second part the same integral is divided by η_2 in case 1 and by η_1 in case 2. Therefore, the TM_z mode contributes with a signal that has a smooth transition at the receiver position and another with a discontinuous rate of change at the interface. Once again, the term responsible for the discontinuity of the derivative presents a ratio of the signals immediately above and below the interface equal to that of the tangent density current field: η_1/η_2.

For the transmitter crossing the interface ($h_0 = 0$),

$$\frac{\partial}{\partial h_0} H_{xx}^{(2)}(r, h_0 + L_z; h_0)\Big|_{h_0=0} = \frac{m}{2\pi r}\left\{\int_0^\infty \frac{k_1^2(u_1 - u_2)}{\eta_1(\mathcal{Z}_1 + \mathcal{Z}_2)} e^{-u_2 L_z} \mathrm{J}_1(\lambda r) d\lambda + \int_0^\infty u_1 u_2 R_{\mathrm{TE}} e^{-u_2 L_z} \mathrm{J}_1(\lambda r) d\lambda - r\int_0^\infty u_1 u_2 R_{\mathrm{TE}} e^{-u_2 L_z} \mathrm{J}_0(\lambda r)\lambda d\lambda\right\}. \quad (25)$$

$$\frac{\partial}{\partial h_0} H_{xx}^{(3)}(r, h_0 + L_z; h_0)\Big|_{h_0=0} = \frac{m}{2\pi r}\left\{\int_0^\infty k_2^2 R_{\mathrm{TM}} e^{-u_2 L_z} \mathrm{J}_1(\lambda r) d\lambda - \int_0^\infty u_2^2 R_{\mathrm{TE}} e^{-u_2 L_z} \mathrm{J}_1(\lambda r) d\lambda + r\int_0^\infty u_2^2 R_{\mathrm{TE}} e^{-u_2 L_z} \mathrm{J}_0(\lambda r)\lambda d\lambda\right\}. \quad (26)$$

The same behaviors are observed and the same conclusions are drawn as in the case of the

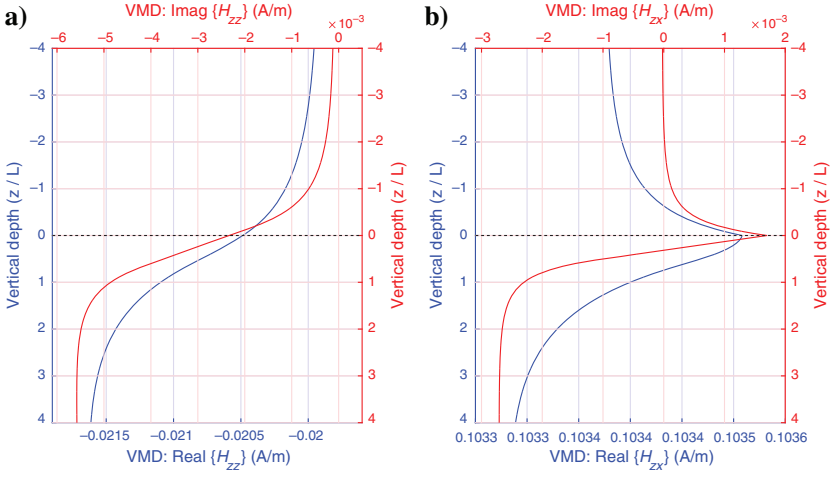

Figure 3. The H_{zz} and H_{zx} from a unit VMD at 20 kHz, source/receiver spacing $L = 1.0$ m, dip angle of 60°, for a two-half-space model with conductivities of $\sigma_{\mathrm{top}} = \sigma_1 = 0.01$ S/m and $\sigma_{\mathrm{bottom}} = \sigma_2 = 1.0$ S/m.

Downloaded 11/15/20 to 177.65.175.205. Redistribution subject to SEG license or copyright; see Terms of Use at https://library.seg.org/page/policies/terms
DOI:10.1190/geo2020-0163.1

receiver transition, which would be expected from the reciprocity and symmetry considerations.

The example shown in Figure 4 is for the same model that generated the curves for the VMD shown in Figure 3 and the logs shown in Figure 1. All of the plots illustrate the conclusions drawn from the analysis of the rate of change of the field with the position of the sonde. Note that the imaginary part of the horizontal component shows two different discontinuities in its derivative: a kink at the transition of the source and a true, albeit small, horn at the transition of the receiver.

To simulate a log of a dipped well, the four components illustrated in Figures 3 and 4 are combined using equations 1 and 2 to generate the coaxial and the coplanar responses shown in Figure 1.

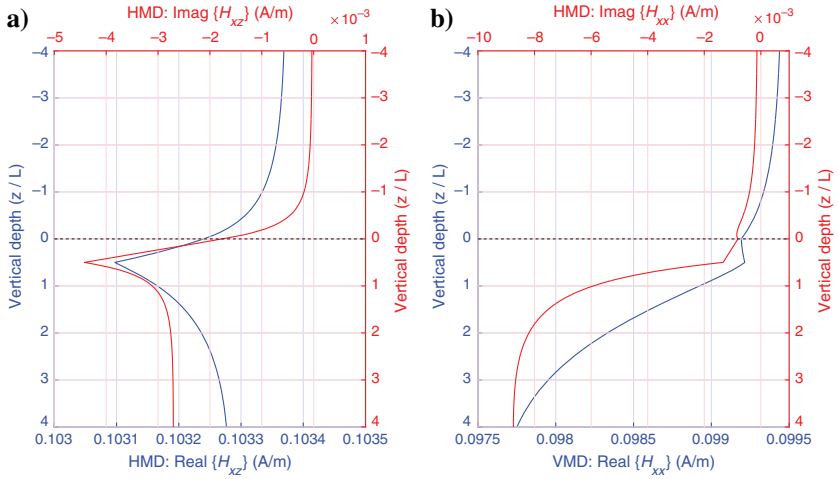

Figure 4. The H_{xz} and H_{xx} from a unit HMD_x at 20 kHz, source/receiver spacing L = 1.0 m, dip angle of 60°, for a two-half-space model with conductivities of $\sigma_{top} = \sigma_1 = 0.01$ S/m and $\sigma_{bottom} = \sigma_2 = 1.0$ S/m.

Geometry of the field lines

The example model shows the changes in the magnitude of the magnetic field with the movement of the tool. Away from the interface, the magnetic field lines follow the dipolar field geometry. The magnitude depends on the conductivity and frequency, but the geometric design of the field lines is the same in both media when considered as an infinite homogeneous space. At the receiver position, the magnetic vector points in the same direction in both media, regardless of the conductivity.

As the tool in medium 1 approaches the interface, the influence of the second medium (shoulder effect) starts to be felt and the magnetic field lines are distorted, so that the magnetic vector at the point receiver changes not only in magnitude but also in direction. After the sonde has passed into medium 2 and distances itself from the interface, the magnetic vector at the position of the point receiver goes back to pointing in the same direction dictated by the geometry of the dipolar field in a homogeneous medium, now with an increased magnitude.

The combined effect of the changing rotations of the magnetic vector and the discontinuity in the current density field imposes the different behaviors observed on the vertical and horizontal components. For example, in this particular model, the H_{zz} component from the VMD increases monotonically, whereas that of the H_{zx} component shows varying behavior, increasing and decreasing as the field vector rotates at the same time as the magnitude changes (Figure 3), all under the influence of the flow of current in the nonhomogeneous medium.

In the case of the HMD_x, the H_{xz} component is analogous to the horizontal one from the VMD and it shows the same pattern of behavior with

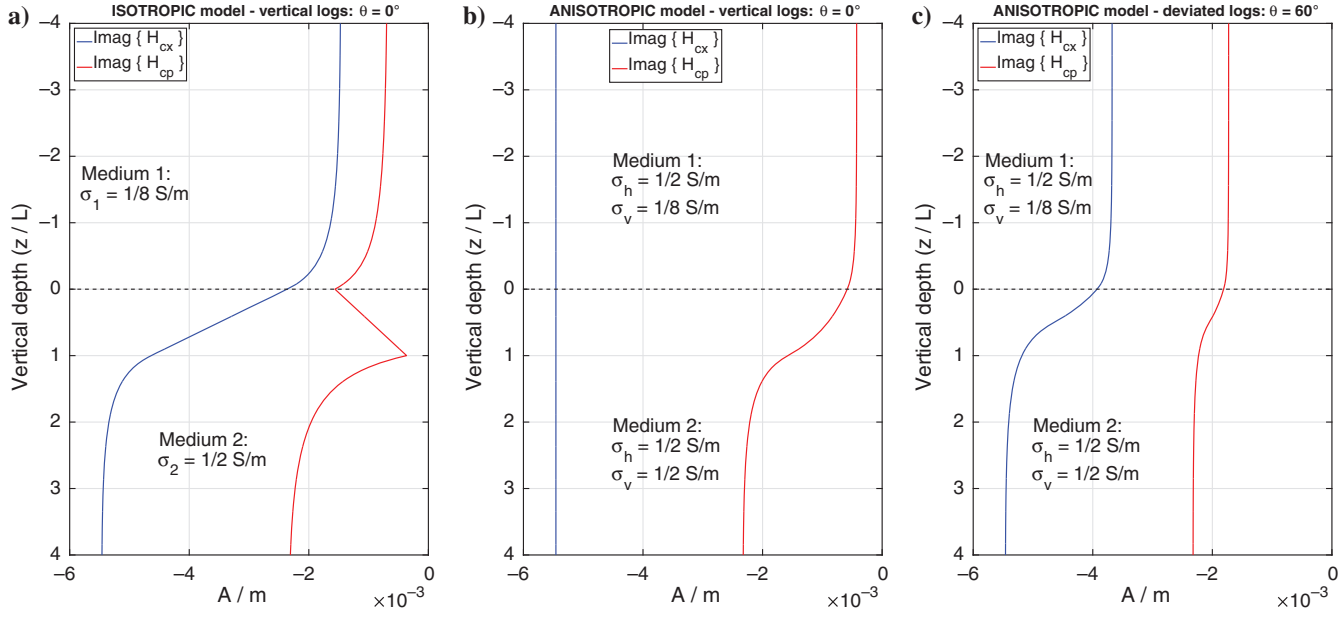

Figure 5. Imaginary magnetic field logs from the coaxial (blue) and coplanar (red) coil arrays within (a) isotropic and (b and c) anisotropic two-half-space models without horizontal conductivity variation.

Downloaded 11/15/20 to 177.65.175.205. Redistribution subject to SEG license or copyright; see Terms of Use at https://library.seg.org/page/policies/terms
DOI:10.1190/geo2020-0163.1

the movement of the sonde. The H_{xx} component presents the most complicated case, with sharp variations in the geometry of the log line at the crossings of source and receiver.

AN ANISOTROPIC EXAMPLE

A last example further illustrates the argument about what is the immediate cause of the horns. Now the bottom half-space is isotropic with conductivity σ_2, and the top half-space is anisotropic with vertical σ_v and horizontal σ_h conductivity components. The particular situation of interest here has the horizontal conductivity equal to that of the bottom medium ($\sigma_h = \sigma_2$) and a contrast in the vertical conductivity ($\sigma_v \neq \sigma_2$). This example has been in the literature for a long time (Moran and Gianzero, 1979; Zhdanov et al., 2001). In this model with homogeneous horizontal conductivity, there will be no discontinuity in the current density field parallel to the interface, regardless of the direction of the dipole source. However, a dipole pointing in any direction other than the vertical will generate electric field components perpendicular to the interface; therefore, there will be a current flow across the interface and surface charges will rise.

To put the following anisotropic case in context, Figure 5a shows the logs of a vertical profile in a two-half-space isotropic model, where $\sigma_1 = 0.125$ S/m and $\sigma_2 = 0.5$ S/m. The logs reproduce the classic characteristics of the two configurations, with a smooth line for the coaxial and unmistakable horns for the coplanar array.

The magnetic field components in a layered anisotropic medium were calculated as described by Kaufman and Ytskovich (2017). The logs in Figure 5b are from a vertical profile in an anisotropic model in which the bottom isotropic half-space has $\sigma_2 = 0.5$ S/m and the top anisotropic medium has $\sigma_v = 0.125$ S/m and $\sigma_h = 0.5$ S/m. Because $\sigma_2 = \sigma_h$ and the fields from the vertical dipole are insensitive to the vertical resistivity, the coaxial line is straight along the whole profile. The coplanar log, however, changes smoothly between the two media, showing no horns nor any discontinuity in its rate of change. In this case, the dipole source is horizontal, so there are electric field components perpendicular to the interface and surface charges appear at the discontinuity of the vertical conductivity. However, because the horizontal conductivity is the same in both media, there is no discontinuous component of the current density field to impose nonsmooth transitions to the logs.

Logs of inclined (60°) profiles in the same model are shown in Figure 5c. Now, the field geometry from both sources gives rise to surface charges, but not to a discontinuous current density field. Therefore, both log curves change smoothly and no horns nor other nonsmooth behavior appear anywhere.

CONCLUSION

We have presented an analysis of the so-called polarization horns that appear in induction logging. The study observes the magnetic components generated by the vertical and horizontal dipoles used in the modeling of induction sondes. The four cases presented here (the vertical and horizontal components from the vertical and horizontal dipole sources) are the ones needed to simulate the responses of the coaxial and the coplanar coil configurations at any dip angle. The analysis was performed by observing the rate of change of each field component with respect to the vertical position of the sonde because it crosses the interface between two homogeneous half-spaces with different conductivities. Each component was calculated in an arbitrary position to account for the deviated angle of the log from the vertical.

The results indicate that, for the VMD, the vertical component is always smooth as the sonde crosses the interface; the horizontal component has a nonsmooth transition (discontinuity in the rate of change and possibly horns, even though in the case of the VMD there is absolutely no surface charge) as the receiver crosses the interface and a smooth transition at the transmitter crossing. For the HMD oriented along the x-axis, the vertical component shows a smooth transition at the receiver crossing, but a discontinuity in its rate of change at the crossing of the transmitter. The horizontal component has influence of the two propagation modes. The transitions for this component are nonsmooth for the transmitter and receiver crossings.

In all cases, the current flow normal to the interface is always continuous, whereas the current tangent to the interface is discontinuous, with a contrast ratio that is equal to those observed in the terms that generate the discontinuities of the rates of change of all components for which a horn or nonsmoothness appears.

Of the four cases, only the horizontal magnetic component from the HMD is under the influence of a vertical current crossing the interface, in which case surface charges appear. However, even in this case the discontinuous part of the rate of change function has the same discontinuity ratio as that of the tangent current density field, which is the contrast ratio of the admittivities of the two media. In no case, the ratio of the rates of change of a field component at the interface is found to be equal to that of the perpendicular electric field associated with surface charges.

Because the magnetic field is generated by the total current density field, and the total perpendicular current is continuous at the interface, we conclude that the horn shapes in the logs cannot be attributed to the influence of surface charges, but are instead associated with the discontinuity of the current density field parallel to the interface between the two media. Further support to this conclusion comes from the anisotropic model, in which there is no change in the horizontal conductivity; hence, there is no discontinuity in the current density and no horns.

Of course, the surface charges, the discontinuity in the current density field, and the geometry of the field lines are all part of the same electromagnetic interaction between the field and the nonhomogeneous medium and therefore are all interrelated. However, our view is that attributing the horn shapes in the logs exclusively to the influence of surface charges misses the bigger picture of that interaction. Putting the emphasis on the component of the current density field that is in fact continuous across the interface instead of recognizing the part played by the discontinuous tangent component misleads and complicates the analysis not only of this reduced model but also of the more realistic cases involving other interfaces, such as well boundary and invasion zones.

ACKNOWLEDGMENTS

The authors thank Petrobras for the support of this research through project number 2017/00424-6 and to the anonymous reviewers whose suggestions helped improve the quality of the manuscript. This paper is dedicated in loving memory to the late O. P. Verma and L. Rijo.

DATA AND MATERIALS AVAILABILITY

Data associated with this research are available and can be obtained by contacting the corresponding author.

Downloaded 11/15/20 to 177.65.175.205. Redistribution subject to SEG license or copyright; see Terms of Use at https://library.seg.org/page/policies/terms
DOI:10.1190/geo2020-0163.1

APPENDIX A

GENERAL EXPRESSIONS FOR THE DERIVATIVES

The VMD

For a VMD placed at the vertical coordinate h_0, the expressions of the vertical magnetic component for the three cases at an arbitrary point receiver position (r, z) are

$$H_{zz}^{(1)}(r,z;h_0) = \frac{m}{4\pi}\int_0^\infty \frac{1}{u_1}\left[e^{-u_1(z-h_0)} + R_{\mathrm{TE}}e^{u_1(z+h_0)}\right]\mathrm{J}_0(\lambda r)\lambda^3 d\lambda, \quad \text{(A-1)}$$

$$H_{zz}^{(2)}(r,z;h_0) = \frac{m}{2\pi}\int_0^\infty \frac{1}{u_1+u_2}e^{u_1h_0}e^{-u_2z}\mathrm{J}_0(\lambda r)\lambda^3 d\lambda, \quad \text{(A-2)}$$

$$H_{zz}^{(3)}(r,z;h_0) = \frac{m}{4\pi}\int_0^\infty \frac{1}{u_2}\left[e^{-u_2(z-h_0)} - R_{\mathrm{TE}}e^{-u_2(z+h_0)}\right]\mathrm{J}_0(\lambda r)\lambda^3 d\lambda. \quad \text{(A-3)}$$

We are looking at the particular case in which the vertical coordinate of the receiver (z) is at a fixed distance from the transmitter, with a vertical separation L_z determined by the fixed dip angle:

$$z = h_0 + L_z. \quad \text{(A-4)}$$

Therefore,

$$H_{zz}^{(1)}(r,h_0+L_z;h_0) = \frac{m}{4\pi}\int_0^\infty \frac{1}{u_1}\left[e^{-u_1L_z} + R_{\mathrm{TE}}e^{u_1(2h_0+L_z)}\right]\mathrm{J}_0(\lambda r)\lambda^3 d\lambda, \quad \text{(A-5)}$$

$$H_{zz}^{(2)}(r,h_0+L_z;h_0) = \frac{m}{2\pi}\int_0^\infty \frac{1}{u_1+u_2}e^{u_1h_0}e^{-u_2(h_0+L_z)}\mathrm{J}_0(\lambda r)\lambda^3 d\lambda, \quad \text{(A-6)}$$

$$H_{zz}^{(3)}(r,h_0+L_z;h_0) = \frac{m}{4\pi}\int_0^\infty \frac{1}{u_2}\left[e^{-u_2L_z} - R_{\mathrm{TE}}e^{-u_2(2h_0+L_z)}\right]\mathrm{J}_0(\lambda r)\lambda^3 d\lambda. \quad \text{(A-7)}$$

To determine the behavior of the measured field components, we find the rate of change of the field as the sonde traverses the interface at $z = 0$. This is accomplished by taking the derivative of the fields with respect to the position h_0 of the transmitter:

$$\frac{\partial}{\partial h_0}H_{zz}^{(1)}(r,h_0+L_z;h_0) = \frac{m}{2\pi}\int_0^\infty R_{\mathrm{TE}}e^{u_1(2h_0+L_z)}\mathrm{J}_0(\lambda r)\lambda^3 d\lambda, \quad \text{(A-8)}$$

$$\frac{\partial}{\partial h_0}H_{zz}^{(2)}(r,h_0+L_z;h_0) = \frac{m}{2\pi}\int_0^\infty R_{\mathrm{TE}}e^{u_1h_0}e^{-u_2(h_0+L_z)}\mathrm{J}_0(\lambda r)\lambda^3 d\lambda, \quad \text{(A-9)}$$

$$\frac{\partial}{\partial h_0}H_{zz}^{(3)}(r,h_0+L_z;h_0) = \frac{m}{2\pi}\int_0^\infty R_{\mathrm{TE}}e^{-u_2(2h_0+L_z)}\mathrm{J}_0(\lambda r)\lambda^3 d\lambda. \quad \text{(A-10)}$$

The expressions for the horizontal component (H_{zx}) in the three cases are

$$H_{zx}^{(1)}(r,z;h_0) = \frac{m}{4\pi}\int_0^\infty \left[e^{-u_1(z-h_0)} - R_{\mathrm{TE}}e^{u_1(z+h_0)}\right]\mathrm{J}_1(\lambda r)\lambda^2 d\lambda, \quad \text{(A-11)}$$

$$H_{zx}^{(2)}(r,z;h_0) = \frac{m}{2\pi}\int_0^\infty \frac{u_2}{u_1+u_2}e^{u_1h_0}e^{-u_2z}\mathrm{J}_1(\lambda r)\lambda^2 d\lambda, \quad \text{(A-12)}$$

$$H_{zx}^{(3)}(r,z;h_0) = \frac{m}{4\pi}\int_0^\infty \left[e^{-u_2(z-h_0)} - R_{\mathrm{TE}}e^{-u_2(z+h_0)}\right]\mathrm{J}_1(\lambda r)\lambda^2 d\lambda. \quad \text{(A-13)}$$

Then, the rates of change of the field at the receiver position ($z = h_0 + L_z$) as the sonde moves are

$$\frac{\partial}{\partial h_0}H_{zx}^{(1)}(r,h_0+L_z;h_0) = \frac{-m}{2\pi}\int_0^\infty u_1R_{\mathrm{TE}}e^{u_1(2h_0+L_z)}\mathrm{J}_1(\lambda r)\lambda^2 d\lambda, \quad \text{(A-14)}$$

$$\frac{\partial}{\partial h_0}H_{zx}^{(2)}(r,h_0+L_z;h_0) = \frac{m}{2\pi}\int_0^\infty u_2R_{\mathrm{TE}}e^{u_1h_0}e^{-u_2(h_0+L_z)}\mathrm{J}_1(\lambda r)\lambda^2 d\lambda, \quad \text{(A-15)}$$

$$\frac{\partial}{\partial h_0}H_{zx}^{(3)}(r,h_0+L_z;h_0) = \frac{m}{2\pi}\int_0^\infty u_2R_{\mathrm{TE}}e^{-u_2(2h_0+L_z)}\mathrm{J}_1(\lambda r)\lambda^2 d\lambda. \quad \text{(A-16)}$$

The $\mathrm{HMD_x}$

The calculation uses Schelkunoff potentials, which allow the separation of the field into the TE_z and TM_z modes of propagation in relation to the z-axis.

Downloaded 11/15/20 to 177.65.175.205. Redistribution subject to SEG license or copyright; see Terms of Use at https://library.seg.org/page/policies/terms
DOI:10.1190/geo2020-0163.1

Considering that $y = 0$ and $\mu_1 = \mu_2 = \mu_0$, the expressions for the vertical magnetic field in the three cases are

$$H_{xz}^{(1)}(r,z;h_0) = \frac{m}{4\pi}\int_0^\infty \left[e^{-u_1(z-h_0)} + R_{\mathrm{TE}}e^{u_1(z+h_0)}\right]\mathrm{J}_1(\lambda r)\lambda^2 d\lambda, \quad \text{(A-17)}$$

$$H_{xz}^{(2)}(r,z;h_0) = \frac{m}{2\pi}\int_0^\infty \frac{u_1}{u_1+u_2}e^{u_1h_0}e^{-u_2z}\mathrm{J}_1(\lambda r)\lambda^2 d\lambda, \quad \text{(A-18)}$$

$$H_{xz}^{(3)}(r,z;h_0) = \frac{m}{4\pi}\int_0^\infty \left[e^{-u_2(z-h_0)} + R_{\mathrm{TE}}e^{-u_2(z+h_0)}\right]\mathrm{J}_1(\lambda r)\lambda^2 d\lambda. \quad \text{(A-19)}$$

Then, making $z = h_0 + L_z$, the rates of change with respect to h_0 become

$$\frac{\partial}{\partial h_0}H_{xz}^{(1)}(r,h_0+L_z;h_0) = \frac{m}{2\pi}\int_0^\infty u_1 R_{\mathrm{TE}}e^{u_1(2h_0+L_z)}\mathrm{J}_1(\lambda r)\lambda^2 d\lambda, \quad \text{(A-20)}$$

$$\frac{\partial}{\partial h_0}H_{xz}^{(2)}(r,h_0+L_z;h_0) = \frac{m}{2\pi}\int_0^\infty u_1 R_{\mathrm{TE}}e^{u_1h_0}e^{-u_2(h_0+L_z)}\mathrm{J}_1(\lambda r)\lambda^2 d\lambda, \quad \text{(A-21)}$$

$$\frac{\partial}{\partial h_0}H_{xz}^{(3)}(r,h_0+L_z;h_0) = -\frac{m}{2\pi}\int_0^\infty u_2 R_{\mathrm{TE}}e^{-u_2(2h_0+L_z)}\mathrm{J}_1(\lambda r)\lambda^2 d\lambda. \quad \text{(A-22)}$$

The expressions for the horizontal magnetic component (H_{xx}) in the three cases, again in the particular case with $\mu_1 = \mu_2 = \mu_0$, are

$$H_{xx}^{(1)}(r,z;h_0) = \frac{m}{4\pi r}\left\{\int_0^\infty \frac{k_1^2}{u_1}\left[e^{-u_1(z-h_0)} + R_{\mathrm{TM}}e^{u_1(z+h_0)}\right]\mathrm{J}_1(\lambda r)d\lambda + \int_0^\infty u_1\left[e^{-u_1(z-h_0)} - R_{\mathrm{TE}}e^{u_1(z+h_0)}\right]\mathrm{J}_1(\lambda r)d\lambda - r\int_0^\infty u_1\left[e^{-u_1(z-h_0)} - R_{\mathrm{TE}}e^{u_1(z+h_0)}\right]\mathrm{J}_0(\lambda r)\lambda d\lambda\right\}, \quad \text{(A-23)}$$

$$H_{xx}^{(2)}(r,z;h_0) = \frac{m}{2\pi r}\left\{\int_0^\infty \frac{k_1^2}{(\mathcal{Z}_1+\mathcal{Z}_2)\eta_1}e^{u_1h_0}e^{-u_2z}\mathrm{J}_1(\lambda r)d\lambda + \int_0^\infty \frac{u_1u_2}{u_1+u_2}e^{u_1h_0}e^{-u_2z}\mathrm{J}_1(\lambda r)d\lambda - r\int_0^\infty \frac{u_1u_2}{u_1+u_2}e^{u_1h_0}e^{-u_2z}\mathrm{J}_0(\lambda r)\lambda d\lambda\right\}, \quad \text{(A-24)}$$

$$H_{xx}^{(3)}(r,z;h_0) = \frac{m}{4\pi r}\left\{\int_0^\infty \frac{k_2^2}{u_2}\left[e^{-u_2(z-h_0)} - R_{\mathrm{TM}}e^{-u_2(z+h_0)}\right]\mathrm{J}_1(\lambda r)d\lambda + \int_0^\infty u_2\left[e^{-u_2(z-h_0)} + R_{\mathrm{TE}}e^{-u_2(z+h_0)}\right]\mathrm{J}_1(\lambda r)d\lambda - r\int_0^\infty u_2\left[e^{-u_2(z-h_0)} + R_{\mathrm{TE}}e^{-u_2(z+h_0)}\right]\mathrm{J}_0(\lambda r)\lambda d\lambda\right\}. \quad \text{(A-25)}$$

Then,

$$\frac{\partial}{\partial h_0}H_{xx}^{(1)}(r,h_0+L_z;h_0) = \frac{m}{2\pi r}\left\{\int_0^\infty k_1^2 R_{\mathrm{TM}}e^{u_1(2h_0+L_z)}\mathrm{J}_1(\lambda r)d\lambda - \int_0^\infty u_1^2 R_{\mathrm{TE}}e^{u_1(2h_0+L_z)}\mathrm{J}_1(\lambda r)d\lambda + r\int_0^\infty u_1^2 R_{\mathrm{TE}}e^{u_1(2h_0+L_z)}\mathrm{J}_0(\lambda r)\lambda d\lambda\right\}, \quad \text{(A-26)}$$

$$\frac{\partial}{\partial h_0}H_{xx}^{(2)}(r,h_0+L_z;h_0) = \frac{m}{2\pi r}\left\{\int_0^\infty \frac{(u_1-u_2)k_1^2}{(\mathcal{Z}_1+\mathcal{Z}_2)\eta_1}e^{u_1h_0}e^{-u_2(h_0+L_z)}\mathrm{J}_1(\lambda r)d\lambda + \int_0^\infty u_1u_2R_{\mathrm{TE}}e^{u_1h_0}e^{-u_2(h_0+L_z)}\mathrm{J}_1(\lambda r)d\lambda - r\int_0^\infty u_1u_2R_{\mathrm{TE}}e^{u_1h_0}e^{-u_2(h_0+L_z)}\mathrm{J}_0(\lambda r)\lambda d\lambda\right\}, \quad \text{(A-27)}$$

$$\frac{\partial}{\partial h_0}H_{xx}^{(3)}(r,h_0+L_z;h_0) = \frac{m}{2\pi r}\left\{\int_0^\infty k_2^2 R_{\mathrm{TM}}e^{-u_2(2h_0+L_z)}\mathrm{J}_1(\lambda r)d\lambda - \int_0^\infty u_2^2 R_{\mathrm{TE}}e^{-u_2(2h_0+L_z)}\mathrm{J}_1(\lambda r)d\lambda + r\int_0^\infty u_2^2 R_{\mathrm{TE}}e^{-u_2(2h_0+L_z)}\mathrm{J}_0(\lambda r)\lambda d\lambda\right\}. \quad \text{(A-28)}$$

REFERENCES

Anderson, B., 2019, You'll never lose a resistivity interpretation argument when James Clerk Maxwell is on your side: The SPWLA Today Newsletter, **2**, 21–24.

Anderson, B., S. Bonner, M. G. Lüling, and R. Rosthal, 1992, Response of 2-MHz LWD resistivity and wireline induction tools in dipping beds and laminated formations: The Log Analyst, **33**, 461–475.

Harrington, R. F., 2001, Time-harmonic electromagnetic fields: IEEE-Press, IEEE Press Series on Electromagnetic Wave Theory.

Howard, A. Q. J., and W. C. Chew, 1989, A variational model of induction logging in a dipping bed environment: IGARSS Symposium, Session F8, paper 5.

Howard, A. Q. J., and W. C. Chew, 1992, Electromagnetic borehole fields in a layered, dipping-bed environment with invasion: Geophysics, **57**, 451–465, doi: 10.1190/1.1443259.

Kaufman, A. A., and G. Ytskovich, 2017, Basic principles of induction logging — Electromagnetic methods in borehole geophysics: Elsevier, 61–63.

Kriegshäuser, B., O. Fanini, S. Forgang, G. Itskovich, M. Rabinovich, L. Tabarovsky, L. Yu, M. Epov, P. Gupta, and J. V. D. Horst, 2000, A new multicomponent induction logging tool to resolve anisotropic formations: Presented at the SPWLA 41st Annual Logging Symposium.

Moran, J. H., and S. Gianzero, 1979, Effects of formation anisotropy on resistivity-logging measurements: Geophysics, **44**, 1266–1286, doi: 10.1190/1.1441006.

Pitcher, J. L., M. S. Bittar, D. Hinz, C. Knutson, and R. Cook, 2011, Interpreting azimuthal propagation resistivity: A paradigm shift: Presented at the SPE EUROPEC/EAGE Annual Conference and Exhibition.

Ward, S. H., and G. W. Hohmann, 1987, Electromagnetic theory for geophysical applications, *in* M. N. Nabighian, ed., Electromagnetic methods in applied geophysics, Vol. 1, Theory: SEG, volume 1 of Investigations in Geophysics, 130–311.

Zhdanov, M. S., W. D. Kennedy, A. B. Cheryauka, and E. Peksen, 2001, Principles of tensor induction well logging in a deviated well in an anisotropic medium: Presented at the SPWLA 42nd Annual Logging Symposium, SPWLA.

Downloaded 11/15/20 to 177.65.175.205. Redistribution subject to SEG license or copyright; see Terms of Use at https://library.seg.org/page/policies/terms
DOI:10.1190/geo2020-0163.1

View publication stats